UNIVERSITY OF TARTU
Faculty of Science and Technology
Institute of Bioengineering

Margaret Pütsepp

SpheraSense: A Software Tool to Automate and Standardize the Analysis of Cancer Spheroid Microscopy Images

Bachelor's Thesis (12 ECTS)

Supervisors:
Tõnis Laasfeld, PhD
Darja Lavõgina, PhD

Tartu 2025

SpheraSense: A Software Tool to Automate and Standardize the Analysis of Cancer Spheroid Microscopy Images

Abstract: In modern data-intensive biological research, making high-throughput image analysis more automated and standardized can improve key aspects of experimental work – reproducibility of results, time cost and expenses. The initiative is particularly beneficial in the research of spheroids, which simulate *in vivo* conditions better than the classical cell culturing model. This thesis presents SpheraSense, a software solution which introduces automation to the analysis of spheroid microscopy images, and includes the application of the software on three cancer spheroid experiments involving small cell lung cancer, head and neck cancer, and glioblastoma. SpheraSense successfully captures significant findings in experimental data, matches manual evaluation variability and reduces analysis time considerably. This thesis streamlines the analysis of spheroid experiments, contributing to more efficient and reproducible research practices.

Keywords: Cancer research, image analysis automation, machine learning, optical microscopy, software development, spheroids

CERCS: B110 Bioinformatics, medical informatics, biomathematics, biometrics; B200 Cytology, oncology, cancerology.

SpheraSense: Vähirakkudest moodustunud sferoidide mikroskoopiapiltide analüüsi automatiseerimise ja standardiseerimise tarkvara

Lühikokkuvõte: Kaasaegses bioloogiaalases teadustöös võimaldab pildianalüüsi laialdasem automatiseerimine ja standardiseerimine parandada eksperimentaaltöö võtmeaspekte – tulemuste reprodutseeritavust, ajakulu ja maksumust. See lähenemine on eriti kasulik sferoidide uurimisel, mis simuleerivad rakkudele *in vivo* tingimusi paremini kui klassikaline rakukultuur. Käesolev töö tutvustab tarkvaralahendust SpheraSense, mis automatiseerib sferoidide mikroskoopiapiltide analüüsi ning hõlmab tarkvara rakendust kolmele sferoidkatsele, mille uurimisobjektiks on väikerakuline kopsuvähk, pea- ja kaelapiirkonna vähk ning glioblastoom. SpheraSense tuvastab edukalt olulisi mustreid katsetulemustes, püsib käsitsi hindamise veapiirides ning vähendab märkimisväärselt katsepiltide analüüsile kuluvat aega. Käesolev töö tõhustab sferoidide analüüsimise protsesse ning panustab uurimismeetodite efektiivsemaks ja reprodutseeritavamaks muutmisesse.

Märksõnad: Vähiuuringud, pildianalüüsi automatiseerimine, masinõpe, optiline mikroskoopia, tarkvaraarendus, sferoidid

CERCS: B110 Bioinformaatika, meditsiiniinformaatika, biomatemaatika, biomeetrika; B200 Tsütoloogia, onkoloogia, kantseroloogia

TABLE OF CONTENTS

ABBREVIATIONS

2D – two-dimensional

3D – three-dimensional

DL – deep learning

DMSO – dimethyl sulfoxide

ECM – extracellular matrix

FBS – fetal bovine serum

GBM – glioblastoma

GUI – graphical user interface

HNSCC – head and neck squamous cell carcinoma

HUVEC – human umbilical vein endothelial cells

ICI – immune checkpoint inhibitor

ITS – insulin, transferrin, selenium

ML – machine learning

NT – non-treated

PBS – phosphate-buffered saline

PI – propidium iodide

ROI – region of interest

ROS – reactive oxygen species

SCLC – small-cell lung cancer

ULA – ultra-low attachment

1. LITERATURE OVERVIEW

1.1 *In vitro* models for cancer research

In 1885, German zoologist Wilhelm Roux conducted a pioneering experiment maintaining chicken embryonic cells in a saline solution, discovering that when provided with the right conditions, cells can survive outside of their native organism [1]. The method, now referred to as *in vitro* cell culturing, has since become a standard platform for experimental work in cell biology.

A significant milestone for oncology in 1951 was the establishment of the first immortal human cell line HeLa, derived from the cervical cancer of Henrietta Lacks at Johns Hopkins Hospital. With HeLa as one of the earliest platforms for sustained and reproducible studies of human cancer biology, cancer cell lines continue to be established [2], leading to massive collaborative projects like the Cancer Cell Line Encyclopedia (CCLE) by Broad institute [3].

Today, a variety of *in vitro* tumor models are available, with techniques continuously evolving to better simulate the natural microenvironment of cells [4]. Importantly, each model captures only a specific set of aspects of the tumor microenvironment, hence the choice of a cancer model to be used in experimental work largely depends on the research objective. Advancing tumor models is essential for accurately simulating tumor behavior and drug responses, providing greater confidence to pursue the development of promising therapies.

1.1.1 Advancing to three-dimensional cell culture systems

The historical standard for cell culture is essentially two-dimensional (2D), consisting of the maintenance of a single cell line as a monolayer on a flat and adherent surface. 2D cell culture has numerous advantages, featuring highly accurate control of experimental conditions, convenience for high-throughput screening and microscopy imaging, along with a comparatively straightforward interpretation of the results. Nevertheless, 2D cultures deviate from *in vivo* conditions in major ways, exhibiting an unrealistically high proliferation rate, altered cellular

behavior, differentiation, gene expression, and drug sensitivity due to the stressful exposure to high stiffness surfaces [5] and trypsinization [6], [7].

Importantly, traditional cell culturing neglects the natural tendency of cells to spatially organize into tissues, which is a critical aspect in shaping biological processes and outcomes. In contrast, the three-dimensional (3D) cell culturing approach proposes culturing cells in tissue mimicking structures, such as spheroids or organoids, to better represent real biological systems [8]. Notably, 3D systems feature environmental gradients of nutrients, drugs, soluble factors, pH, oxygen, and waste products, creating distinct microenvironments for cells organized into layers. Resultingly, the culture becomes heterogeneous in terms of cell cycle phases and proliferation rate.

3D cell culture systems can broadly be categorized into scaffold-based and scaffold-free models. Scaffold-based models provide the cells with a 3D adhesion and growth environment, encouraging the cells to build larger structures and interact with the extracellular matrix (ECM) – the ECM is naturally produced by the cells and provides mechanical support, impacts cell differentiation, proliferation and apoptosis. In oncology, the cells remodeling their surrounding ECM provides insights into processes like migration or invasion [9]. To promote physiologically relevant ECM deposition and dynamics, scaffold-based models employ hydrogels (synthetic or natural), solid scaffolds (porous or fibrous) and decellularized tissue [10].

Scaffoldless models, on the other hand, grow cells in a continuously suspended manner, encouraging self-aggregation into spheroids. Scaffoldless approaches employ attachment-resistant surfaces, which is the case for ultra-low attachment plates or the hanging drop technique, or induce flotation mechanically via magnetic levitation or culture vessel rotation. Other hybrid methods for achieving multi-layered cellular structures incorporate coculturing, transwell-based or microfluidic systems and bioprinting [5], [11], [12].

Shortcomings of 3D models include limited options for imaging and analysis techniques, also the complex interpretability and reproducibility of results due to many variables. As of today, 3D cell culturing stands to benefit significantly from the standardization of protocols and improved reproducibility, reinforcing the 3D approach as the emerging norm for *in vitro* testing.

1.1.2 Spheroid cultures

Spheroid cultures are a subset of 3D cell culturing models, being one of the most straightforward and high-throughput choices to reap the benefits of 3D culturing. When devoid of a surface to attach to, cells form spherical aggregates, usually ranging from 50–1000 μm in diameter. In cancer studies, the proclivity or failure of cells to aggregate is an informative biological insight into tumor behavior and response to therapies. Drug screening typically involves the induction of spheroid formation and incubation with a drug, followed by measurement of cell survival, spheroid morphology and growth kinetics [13].

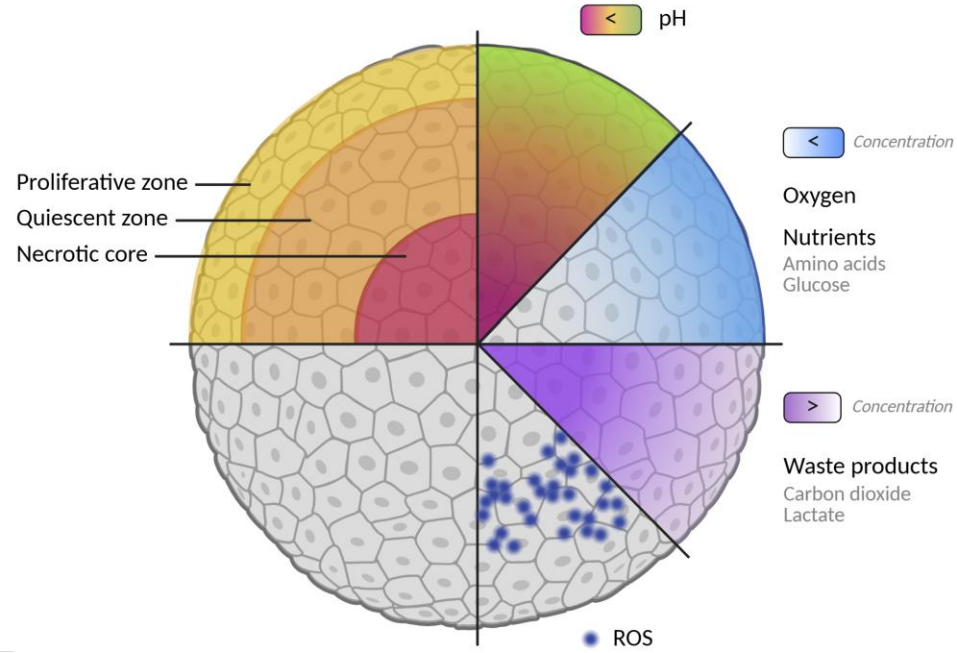

Figure 1. Schematic representation of concentration gradients in a spheroid. Cell proliferation varies in response to local stressful or favorable conditions experienced by the cells. Oxygen concentration (approximate range 2.5–65 mmHg)[14] and nutrient availability decrease toward the spheroid core due to diffusion limitations. pH levels also shift (range 6.0–7.4)[15], [16], becoming more acidic towards the spheroid core, but reflect a combination of diffusion and metabolic effects, such as the accumulation of waste products CO_2 and lactate. Metabolic activity also affects ROS (reactive oxygen species) production, the distribution of which is highly localized due to a short half-life (nanoseconds to seconds).

Illustrated in Figure 1, spheroids with diameters over 200–500 μm develop oxygenation and nutrient gradients [17], impacting cell proliferation. The outermost cells benefit from exposure to oxygen and nutrients, whereas the inner structures experience a buildup of metabolites, acidity,

reactive oxygen species (ROS), culminating in necrotic spheroid cores due to hypoxia (pO_2 < 2.5 mmHg) [18]. In oncology, hypoxia is particularly significant due to its impact on gene expression related to cell survival, promoting an invasive and quiescent tumor cell population that is stress and therapy resistant [18]. Spheroid cultures are also a great platform to study drugs impacting cell signaling, cell-cell contacts [17] and the drug diffusion process in tissues [19]. The diffusion of drugs is influenced by spheroid architecture, which in turn is modified by drug response, resulting in a reciprocal, dynamic interaction.

A variety of cell lines can be used for spheroid formation, widely used cancer cell lines include A549 (lung cancer), U87-MG (glioblastoma), and MCF-7 (breast cancer), whereas non-cancerous lines employ HUVECs (endothelial cells) or fibroblasts. Among these, epithelial-derived lines tend to form denser, more compact spheroids due to the presence of tight junctions [20]. Such structural differences highlight the importance of empirically optimizing cell culturing conditions for the individual cell lines to produce spheroids in uniform sizes.

1.2 Cancer treatment methods used in this work

1.2.1 Irradiation

Irradiation with a medical linear accelerator (LINAC) employed in the small cell lung cancer (SCLC) experiment is a widely used anti-cancer treatment that damages the DNA of cancer cells. Radiation therapy is typically prescribed concurrently with chemotherapy, using either once-daily or twice-daily fractionation schedules, with total doses ranging from 45 to 70 Gy for SCLC [21]. Irradiation applied to cancer spheroids affects both cell proliferation and morphology, enabling to study potential treatment response or resistance, optimizing therapeutic efficacy [22].

1.2.2 Immune checkpoint inhibitors

Pembrolizumab and nivolumab are agents of immunotherapy, aiming to leverage the patient's own immune system to combat disease. One of the tactics of cancer to evade immunosurveillance is suppressing the immune response through upregulating the PD-1/PD-L1 pathway [23].

Programmed death 1 (PD-1) is an immune checkpoint receptor expressed on the membrane of the immune system cells that binds to the ligands PD-L1 and PD-L2 expressed on the membrane of the cancerous cells. This binding event inhibits T cell activation and cytotoxic activity [24], and in the context of a healthy organism, is thought to contribute to self-tolerance, preventing autoimmune reactions.

Immune checkpoint inhibitors (ICIs) are a class of therapeutics that block checkpoint proteins. ICIs pembrolizumab (Keytruda) and nivolumab (Opdivo) are IgG4 monoclonal antibodies (mAbs) that block the PD-1/PD-L1/2 interaction, restoring T cell activity against cancerous cells [25] [26]. The possible impact of antibodies onto the cancerous cells alone has been, however, less studied, although recent reports have indicated that ICIs can modulate the response of the cancerous cells to chemotherapy *via* yet unknown mechanisms [27], [28]. The ICIs used within this study were tested at concentrations corresponding to the steady-state levels in the patient's blood [29].

1.2.3 Targeted and chemotherapeutic drugs

Onametostat and lomustine represent two distinct classes of anticancer agents with therapeutic effect on glioblastoma. Onametostat is an epigenetic modulator that inhibits the enzyme PRMT5 (Protein Arginine Methyltransferase 5), disrupting the splicing of genes related to cell cycle regulation, survival, and differentiation, thereby impairing tumor cell stemness and proliferation [30], [31]. Lomustine, on the other hand, is a cytotoxic DNA-alkylating agent that induces DNA cross-linking and damage, triggering apoptosis in proliferating tumor cells [32].

Important to the onametostat and lomustine experiment, the glioblastoma cell lines U-251 and U-87 were chosen due to their different MGMT (O^6-methylguanine-DNA methyltransferase) expression status, which affects resistance to chemotherapy [33]. MGMT is a DNA repair enzyme that removes alkyl groups from guanine, protecting cells from the cytotoxic effects of alkylating agents such as lomustine. MGMT-positive (U-251 MG) cells are therefore typically more resistant to alkylating agents, whereas MGMT-negative (U-87 MG) cells are more sensitive to such therapies.

1.3 Bioimage analysis

Bioimage analysis refers to the extraction of biological information from imaging data, *e.g* microscopy images in a way that is quantitative, reproducible and as unbiased as possible. Although bioimage analysis workflows can get very complex, the core aims are finding relevant metrics which describe the experimental results and providing an accurate method for their quantification. Given that up to 70% of the experiments in clinical research and pharmaceutical development generate images, bioimage analysis proficiency is becoming increasingly important in the field of biological sciences and research [34].

1.3.1 Bioimage analysis process

Typical steps of the bioimage analysis process (Figure 2) involve image preprocessing, object segmentation, feature extraction and quantification [35]. Preprocessing of raw images incorporates quality control and noise reduction, often achieved using image filters such as Gaussian, bilateral, and non-local means filters. Object segmentation uses image morphology operations and thresholding to assign a label to each pixel, detecting (or separating different objects into) regions of interest (ROIs). Feature extraction analyses different characteristics of the ROI, producing the quantitative data needed for bioimage interpretation and experimental conclusions.

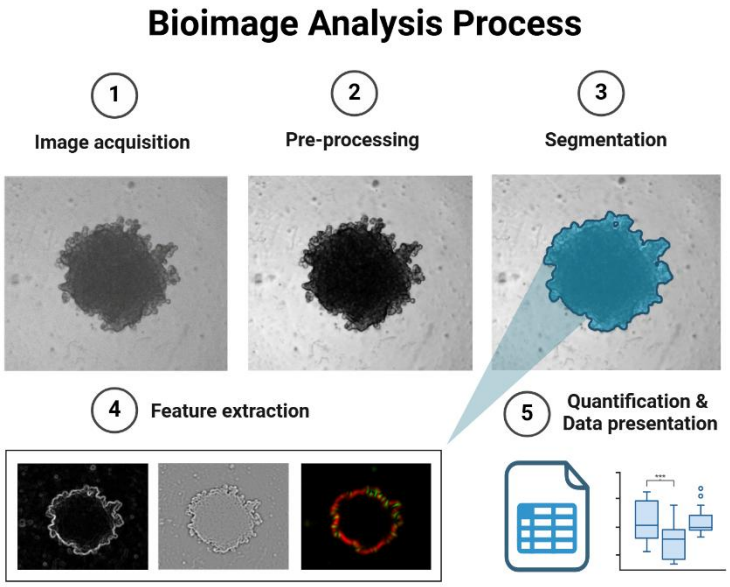

Figure 2. A generalized example of a bioimage analysis workflow. Pre-processing (2) involved noise reduction, contrast and edge enhancement, and the extracted features (4) are based on (from left to right) Gaussian gradient magnitude, Laplacian of Gaussian and structure tensor eigenvalues.

1.3.2 Feature capture and engineering

Features are measurable characteristics of the image, computed from pixel values within regions of interest and broadly classified as either pixel-level or object-level features. Pixel-level features capture properties such as color and texture – color features quantify color spread, prominence, and co-occurrence, whereas texture features quantify image sharpness, contrast, intensity changes or edges [36]. Object-level features describe properties of larger regions, characterizing area, shape, connectedness, and density among others [36].

Feature engineering encompasses the selection, transformation and optimization of these features to enhance their robustness for downstream analysis [37]. Features can, for example, be normalized, weighted, correlated or aggregated into ensemble features [38]. In bioimage analysis, the overarching goal of the process is to extract reproducible feature patterns that yield biological insights. Importantly, feature sets should avoid redundancy and reflect the nature of the experiments, returning expected results, *e.g* classification or regression targets.

1.3.3 Machine learning in image analysis

Integrating machine learning (ML) into the image analysis pipeline can aid in capturing complex patterns in images and greatly enhances throughput, particularly in image segmentation and feature exploration stages. Classical ML algorithms, such as support vector machines, random forests, K-nearest neighbors and gradient boosting, operate on structured feature sets and typically return labeled image data, such as classified pixels or objects [39]. The model performance and generalizability in this case depends heavily on the quality of feature engineering. In contrast, deep learning (DL) models require no curated feature sets as they learn feature patterns directly from raw images, but require extensive labeled data for training, pose high computational demands and are complex to interpret [40]. Other limitations relevant for both ML and DL approaches include bias and overfitting, especially in the case of training on limited, class imbalanced or noisy data.

1.4 Software used in this work

1.4.1 MATLAB

Originally developed by Cleve Moler in the 1970s [41], MATLAB (MATrix LABoratory) is a high-level language optimized for scientific matrix and array computations. Its suitability for image data processing, combined with a user-friendly environment for simple application prototyping and distribution, made it the preferred platform for developing SpheraSense. Regarding add-ons, SpheraSense uses the 'Image Processing Toolbox' and the 'Statistics and Machine Learning Toolbox' in its operation.

1.4.2 Ilastik

Ilastik [42] is an open-source software application that provides a graphical user interface (GUI) for common bioimage analysis workflows, including image classification, segmentation, and object tracking. The Pixel Classification workflow used in this work supports various classifier types—such as random forests, k-nearest neighbors, and Gaussian naïve Bayes—and offers a

range of image filters to detect pixel-level features, including color, intensity, edge information, and texture. The machine learning model training process is user-friendly, allowing intuitive annotation that guides the ML predictions. Once trained, the model is suitable to be applied to novel bioimage datasets, generating probability maps, feature maps, and label predictions as output.

1.4.3 Fiji

Fiji [43] is an open-source image processing software built on ImageJ [44], and similarly provides a wide range of tools for bioimage analysis. It supports various functionalities such as image segmentation, measurement, and visualization, also benefitting from a powerful plugin architecture. In the context of this work, Fiji was used for manual image quantification.

1.4.4 Other tools

For data analysis and graphing purposes, GraphPad Prism 8.4.2 and Excel 2024 were used. The illustrating figures were made with BioRender [45].

2. RESEARCH QUESTIONS

To enhance standardization and harness machine learning in spheroid image analysis, the software tool SpheraSense was developed as a dedicated solution. The present work was aimed at answering the following research questions:

1. Can SpheraSense analysis achieve an error rate that is comparable to human judgement variability when using manual image tracing in Fiji?
2. How much time is SpheraSense able to save with batch processing compared to manual analysis?
3. Can SpheraSense be integrated into the pre-existing laboratory workflows?

3. SOFTWARE DEVELOPMENT

Preexisting spheroid research workflows typically consist of laboratory experiments, results imaging and data analysis. SpheraSense assists researchers in the stage of image quantification and integrates into the workflow as illustrated in Figure 3.

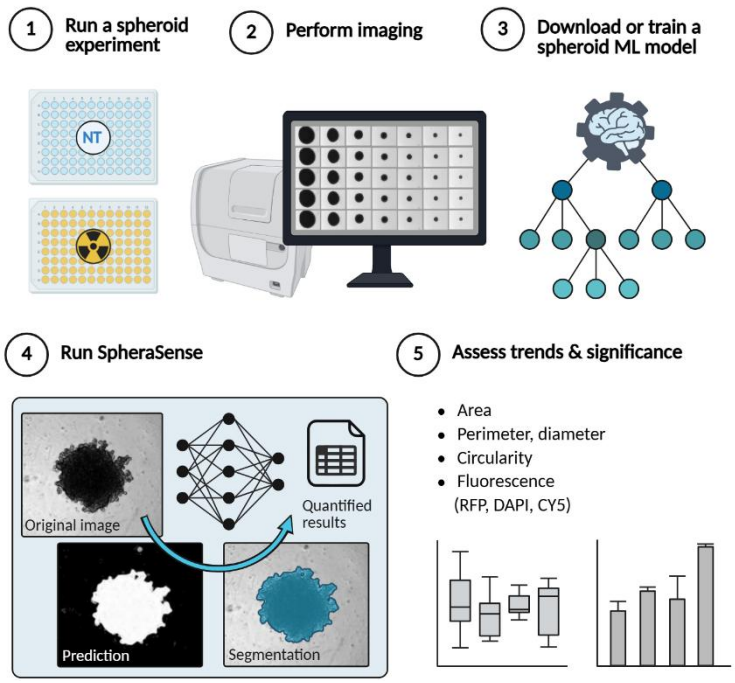

Figure 3. Schematic of the workflow and quantification employed in the scope of this work.

Designing the main functionality of the software, the requirements were the following:

1. Read 96-well plate microscopy images (with associated metadata) into a unified database.
2. Support multiple imaging channels: Bright Field, DAPI, RFP, CY5.
3. Load and utilize pretrained machine learning models in the HDF5 format to segment spheroid microscopy images.
4. Quantify morphological and intensity-based metrics: spheroid area, perimeter, diameter, circularity, and fluorescence intensity.

5. Provide an intuitive GUI for image browsing and quantification visualization, enable the user to make corrections to quantification and add notes to images.
6. Support batch processing of large datasets.
7. Export quantified data as an Excel or CSV file for subsequent analysis.
8. Be easily sharable and customizable to fit the needs of other research groups.

SpheraSense imports image data from TIFF format images along with the stored metadata, then sorts and stores the images according to the 96-well plate format. The metadata encompasses details such as the imaging instrument specifications, acquisition parameters, and the time and date of image capture. In the context of SpheraSense, the imaging scale and well ID values are fetched from metadata and multi-channel support is achieved through regex-based sorting and loading of the images. SpheraSense is suitable to comfortably browse 96-well experiments by navigating across well IDs, Z-planes and imaging channels. The interface and user guide are provided in Annex 4, Figure 18.

In the image quantification step, SpheraSense applies a spheroid recognizing ML model using Ilastik, accessed and run via the command-line interface in headless mode. This step outputs a probability map that represents pixel-wise classification confidence, and identifies the spheroid as the ROI. Morphological and intensity-based metrics are then quantified from the classified region. The ML model used to quantify the spheroid experiments in this work was produced by using the Pixel Classification workflow with Random Forest as its classifier type and 70 bright-field microscopy images of spheroids in the training set. Training was carried out using the human-in-the-loop concept such that pixels with the highest prediction uncertainty were labeled as a priority for model learning efficiency.

The primary goals of the development process were to ensure that SpheraSense delivers reproducible results, achieves statistical agreement with manual quantification, and substantially reduces analysis time compared to the manual approach. Post-quantification data analysis and visualization are deliberately excluded from the core scope of the software, providing researchers with the flexibility to apply analytical methods that align closely with their experimental objectives.

4. EXPERIMENTAL SECTION

In the scope of this work, three cancer spheroid experiments were performed, utilizing small cell lung cancer (SCLC), the head and neck squamous cell carcinoma (HNSCC) line FaDu and two cell lines of glioblastoma (GBM). While the SCLC experiment was performed by the present author, all the cancer spheroid experiments had been previously carried out by Associate Professor Darja Lavõgina in the laboratory of Professor Ago Rinken, in the Institute of Chemistry of the University of Tartu. Radiation exposure was conducted together with Helen Lust, using a radiotherapy machine Varian TrueBeam 2.5 (Varian Medical Systems, CA, USA), which was operated by MSc. Markus Vardja at the Tartu University Hospital.

4.1 SCLC spheroid treatment with irradiation

Cell culturing

The small-cell lung cancer cell line CRL-5853 (ATCC, USA) was grown in a 10 cm Petri dish (BioLite 130182, Thermo Fisher Scientific, USA) in phenol-red containing Dulbecco's Modified Eagle/Ham's F-12 (DMEM/F-12) medium (1:1; Corning, USA), with 5% fetal bovine serum (FBS; Capricorn Scientific, Germany), Insulin-Transferrin-Selenium (ITS-H; Capricorn Scientific, Germany) and hydrocortisone (H6909, Sigma-Aldrich, USA) until ~90% confluence. The cells were then trypsinized according to standard protocol, resuspended in regular growth media and seeded into two 75 cm^2 adherent flasks (TPP, Switzerland), 9.7×10^6 cells per flask. The flasks were then incubated in standard conditions (37 °C, 5% CO_2) for 24 hours in a humidified incubator (Sanyo, Japan).

Treatment and plating

After incubation, one T75 flask was irradiated with 2 Gy and allowed to recover for 30–60 minutes, the second flask served as non-treated (NT) control. Cells of both flasks were then trypsinized and resuspended in growth media, yielding 9 mL of cell suspension each. Cell counting with the TC-

10 cell counter (Bio-Rad, USA) revealed 0.92×10^6 cells/mL for the non-irradiated flask and 0.70×10^6 cells/mL for the irradiated flask.

SCLC cells were then plated on an ultra-low attachment (ULA) plate (Corning 4515; Corning, USA), with the plating scheme illustrated in Annex 1, Figure 10. To minimize edge effect, the outermost wells of the plate were filled with phosphate buffered saline (PBS) and to mitigate the effects of different cell counts, control cell suspension was diluted with media to approximate the cell count of the irradiated cell suspension. In the second column, 400 µl of cell suspension was added to each well; NT cell suspension in wells B2, C2, D2 and the irradiated cell suspension in wells E2, F2 and G2. Two-fold serial dilutions of the cell suspensions were then performed across columns 3–11, yielding cell seeding densities of 200–1.05×10^5 cells for spheroid formation. The plate was then incubated for two days.

Imaging settings

After 48 and 72 hours from seeding, spheroid formation on the ULA plate was assessed using a Cytation 5 multi-mode reader (BioTek; Winooski, VT, USA) under 37 °C and 5% CO_2 conditions. Microscopy used a 4× magnification lens (1.613 µm/pixel) and autofocus with optional scan. The image acquisition settings were the following: for bright-field channel imaging, LED intensity was 5 (scale 1–10), integration time 100 ms and detector gain 3 (scale 0–24); for RFP channel (excitation wavelength 531 nm, emission wavelength 593 nm) imaging, LED intensity was 5, integration time 350 ms and detector gain 15. Z-stack imaging was performed across nine slices with four slices above and below the autofocus level and 50 µm between the Z-planes, resulting in a 400 µm thick Z-stack.

Propidium iodide staining

After imaging, propidium iodide staining of necrotic/late apoptotic cells was performed by adding a final concentration of 2 µg/mL propidium iodide (Acros Organics, Switzerland) to each well and incubating for 30 minutes. Post-incubation images were taken at one autofocused level using the RFP imaging settings as described above.

4.2 HNSCC spheroid treatment with pembrolizumab and nivolumab

Cell culturing

FaDu cells (HTB-43; ATCC, USA) were cultivated, trypsinized from the original growth vessel, and added to Eagle's Minimum Essential Medium (EMEM; ATCC, USA) with 10% FBS (Capricorn, USA), yielding 6 mL of cell suspension with 1.5×10^6 cells/mL.

Treatment and plating

Pembrolizumab (Keytruda; Merck & Co., USA) and nivolumab (Opdivo; Bristol-Myers Squibb Pharma, USA) were employed in this experiment. The antibodies were plated on a 96-well U-bottomed plate (Greiner Bio-One, Austria) before the addition of FaDu cells, so as to not disturb spheroid formation dynamics, and the plating scheme is provided in Annex 2, Figure 12.

The outermost wells of the plate were filled with PBS with the rest filled with 150 µL of medium. Rows B and C of the plate were left as non-treated control, whereas drug treatment was added to the rest of the cell suspensions - pembrolizumab to rows D, E in the final concentration of 0.09 mg/mL, and nivolumab to rows F and G in the final concentration of 0.13 mg/mL.

Then, FaDu cells were added to rows B–G. The column 2 was filled with 300 µL of the cell suspension and two-fold dilutions were performed across columns 2–11, resulting in seeding densities ranging from 450–2.25×10^5 cells per well. The plate was then incubated in standard conditions.

Imaging

Plate imaging was performed on the spheroid plate 72 hours and 96 hours after treatment with ICIs, using the bright-field channel with the imaging settings described in the SCLC experiment.

4.3 GBM spheroid treatment with onametostat and lomustine

This experiment was a part of a previously published larger study on inhibitors targeting the cell cycle-regulating kinases and the epigenetic writers/erasers [31]. Relevant to this thesis, the effects of onametostat and lomustine on glioblastoma spheroid culture were studied.

Cell culturing

The glioblastoma cell lines U-251MG and U-87MG (ATCC, USA) were grown in EMEM (ATCC, USA), containing Earle's Balanced Salt Solution, non-essential amino acids, 2 mM L-glutamine, 1 mM sodium pyruvate, and 1500 mg/L sodium bicarbonate. Onametostat and lomustine (Selleckchem, Germany) used were originally in concentrations 20 mM and 50 mM, respectively. DMSO was obtained from AppliChem, Germany and propidium iodide from Acros Organics, Switzerland.

Treatment and plating

Treatment was plated on a 96-well ULA plate (Thermo Fisher Scientific, USA) before the addition of GBM cells, so as to not disturb spheroid formation dynamics, and the plating logic is illustrated in Annex 3, Figure 15. The outermost wells were filled with PBS and in Eppendorf tubes, the following solutions were prepared: 1) ~1500 µL of 0.1% DMSO, 2) ~2000 µL of 40 µM onametostat, 3) ~1500 µL of 100 µM lomustine. Columns 2 and 7 of the ULA plate were filled with 0.1% DMSO as a negative control. Onametostat was plated in three final concentrations – 20 µM in 3. and 8. columns, 2 µM in 4. and 9. columns, 0.2 µM in columns 5 and 10. Lomustine (50 µM) was added to columns 6 and 11.

GBM Cells were then added to the plate. Cell line U-251 was trypsinized, counted using TC-10 cell counter (Bio-Rad, USA) and seeded into columns 2–6, with the wells each having a cell count of 2500 and 100 µL of media. U-87 cells were seeded into columns 7–11 by the same protocol. The cells were then grown in standard incubation conditions. At the timepoint of 48 hours, the media of the plate was changed to be identical to the original treatment, and the incubation was continued until 96 hours.

Propidium iodide treatment and imaging

At 95 hours of incubation, propidium iodide staining was performed – PI solution in PBS was added to all wells to a final concentration of 2 µg/mL and the plate was incubated for an additional hour before imaging. Imaging was thus carried out at 72- and 96-hour timepoint with the settings described in the SCLC experiment, capturing the images in bright-field and RFP channels across nine Z-planes.

4.4 Data analysis methods

The microscopy images from the experiments were analyzed both manually and with SpheraSense, both approaches assessing spheroid area, perimeter and circularity. Manual quantification was performed using Fiji – the spheroid contour was traced with the "Freehand selection" and the "Measure" tool extracted the area, perimeter and circularity of spheroids. Circularity (C) is computed using the perimeter (P) and area (A) of the object (formula 1).

$$C = \frac{4\pi A}{P^2} \tag{1}$$

To quantify the discrepancy of results that manifest between different people performing manual analysis, the coefficient of variation (CV) was calculated – defined as the ratio of the standard deviation (σ) to the mean (μ) and expressed as a percentage (formula 2). The statistic is also known as normalized root-mean-square deviation (RMSD) or percent RMS.

$$CV = \frac{\sigma}{\mu} \times 100\% \tag{2}$$

To assess how different, on average, SpheraSense results were from manual analysis, the mean absolute percentage error (MAPE) was used, which quantifies the average absolute difference between manual (y_i) and software estimated datapoints ($\hat{y}_i$) in percent (formula 3).

$$MAPE = \frac{1}{n}\sum_{i=1}^{n}\left|\frac{y_i - \hat{y}_i}{y_i}\right| \times 100\% \tag{3}$$

Statistical tests used for determining significance in quantified results included the unpaired t-test, the Mann-Whitney U-test and the ordinary one-way ANOVA.

5. RESULTS

5.1 Results of the SCLC experiment

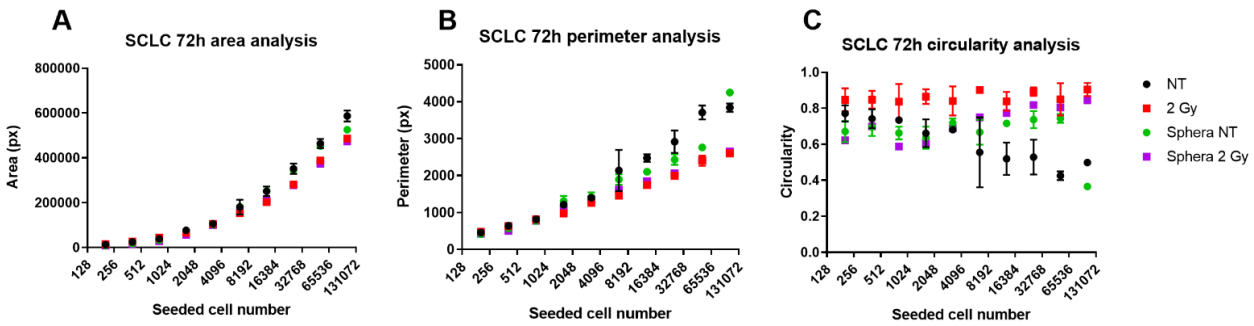

Figure 4. Small-cell lung cancer spheroid area (A), perimeter (B) and circularity (C) dependence on the number of seeded cells, assessed at 72 hours both by manual analysis (NT & 2 Gy) and with SpheraSense analysis (Sphera NT & Sphera 2 Gy). The imaging scale was 1.613 µm/pixel and 2 Gy indicates the dose of radiation the treated cells were subjected to. The data points plotted are an average of n = 3 measurements and the error bars are based on standard deviation.

72 hours post seeding (48 hours after irradiation) of small cell lung cancer cells, spheroid area, perimeter and circularity were assessed across different cell seeding densities, both manually and using SpheraSense (Figure 4). The microscopy images, which were the basis of the measurements, are provided in Annex 1, Figure 11.

As expected, higher cell seeding densities lead to proportionally larger spheroids, a trend seen in the area (Figure 4.A) and perimeter (Figure 4.B) data. Notably, however, irradiated spheroids compared to their non-treated (NT) counterparts showed a lower sensitivity to increased cell seeding density with respect to the effect on area and perimeter. To add, the more pronounced reduction in perimeter growth indicates a shift toward a more compact spheroid morphology under irradiation, which may also be caused by cell death.

Further looking at circularity (Figure 4.C), irradiated spheroids were consistently more circular than non-treated controls, which in turn became less circular as cell density increased. The experiment indicates that the natural inclination of the SCLC cell line is to form rather non-

compact spheroids with an irregular perimeter profile, whereas irradiation makes spheroids more compact and circular (formula 1).

The SCLC spheroids were also imaged in the RFP channel to quantify the effect of propidium iodide staining, a marker indicating cell death. The PI fluorescence intensity was, however, insignificant – the mean pixel intensity values mostly clustered around 3500, whereas previous experiments with considerable cell death have involved mean RFP intensity values up to 10 000.

Regarding SpheraSense performance, the software produced result trends were very similar to manual assessment of area and perimeter, particularly in irradiated spheroids. With respect to significant differences ($p < 0.05$) in NT versus treated spheroids (Figure 5), both manual and software analysis captured significant changes in spheroids seeded with 1.3×10^5 cells regarding spheroid area ($p = 0.018$), perimeter ($p = 0.0006$) and circularity ($p = 0.0062$). Interestingly, differing from manual analysis, SpheraSense found a significant ($p = 0.029$) difference in the perimeter of 6×10^4 cell spheroids, and on the other hand, deemed the circularity change of 6×10^4 cell spheroids insignificant ($p = 0.125$), although the manual analysis resulted in a p value of 0.037.

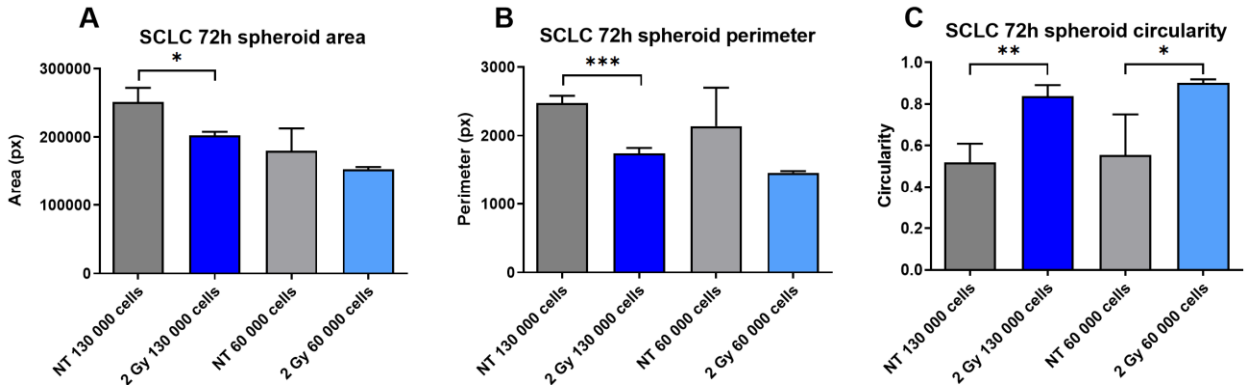

*Figure 5. Manual analysis of 130 000 and 60 000 cell SCLC spheroids 48 hours post irradiation with 2 Gy). The imaging scale was 1.613 µm/pixel, the bar plot values are an average of n = 3 measurements, and the error bars are based on standard deviation. Regarding significance assessed by the Mann–Whitney U-test, "***" indicates a p value of ≤ 0.001, "**" indicates p ≤ 0.01, and "*" stands for p ≤ 0.05.*

Regarding possible biological interpretation of the experiment, irradiation of 2 Gy could be altering cell-cell interactions or reducing invasive behavior, resulting in more compact structures.

These findings are consistent with research on radiation-induced modulation of cancer cell behavior, with 2 Gy being a commonly prescribed dose of radiation in treating cancerous tumors.

5.2 Results of the HNSCC experiment

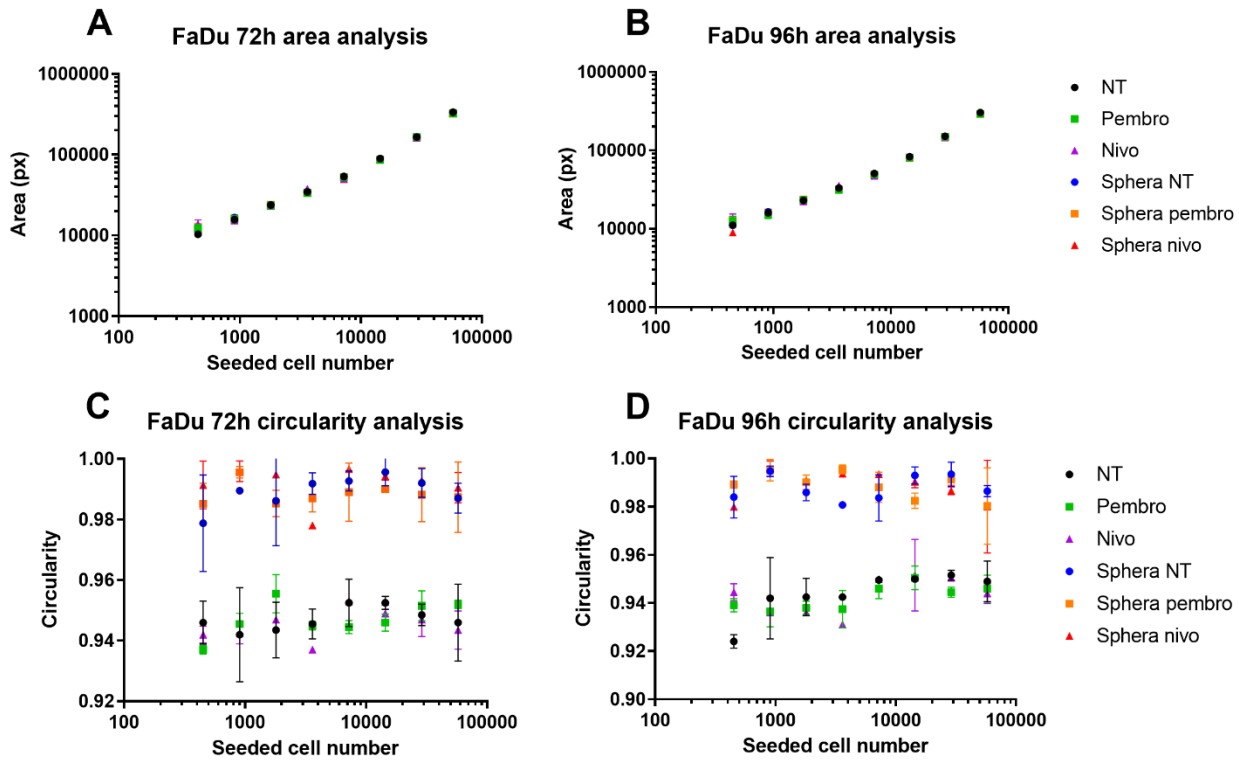

Figure 6. FaDu spheroid area (A, B) and circularity (C, D) at 72 and 96 hours after treatment with pembrolizumab and nivolumab, assessed both manually and with SpheraSense (Sphera). The imaging scale was 1.613 µm/pixel, the data points plotted are an average of n = 2 measurements and the error bars are based on standard deviation. NT stands for non-treated, "Nivo" for nivolumab and "Pembro" for pembrolizumab treatment.

The area and circularity of HNSCC spheroids were quantified 72 and 96 hours post treatment with pembrolizumab and nivolumab (Figure 6). Notably, the FaDu cell line formed spheroids which were highly structurally cohesive and round (Annex 2, Figure 13 and 14), with minimum circularity of 0.922 and a value of 1 indicating a perfect circle.

Spheroid area was proportionally bigger with higher cell count at both timepoints as expected. However, the experiment data showed no significant difference between drug treated and negative control spheroids, suggesting that pembrolizumab and nivolumab, at least in tested concentrations, do not meaningfully affect spheroid size or circularity within 96 hours.

This experiment provided an insight that nivolumab and pembrolizumab alone do not have an impact on FaDu spheroid formation and development. This may be attributed to the fact that ICI type drugs function by impacting the immune cells of the body, absent in this experiment. Future studies can therefore exclude the direct effect of pembrolizumab and nivolumab on cancer cells, allowing for the exploration of combination therapies. A technical conclusion from the experiment is an optimized cell count for the FaDu cell line.

5.3 Results of the GBM experiment

The area and circularity of U-251 and U-87 glioblastoma spheroids were quantified 72 hours (Figure 7) and 96 hours (Figure 8) post-treatment with onametostat or lomustine, with the assessment of cell death *via* propidium iodide staining at the latter timepoint. Notably, the U-87 cell line formed spheroids which were significantly bigger and less compact compared to the spheroids of U-251, with the microscopy imaging results in Annex 3, Figure 16 and 17.

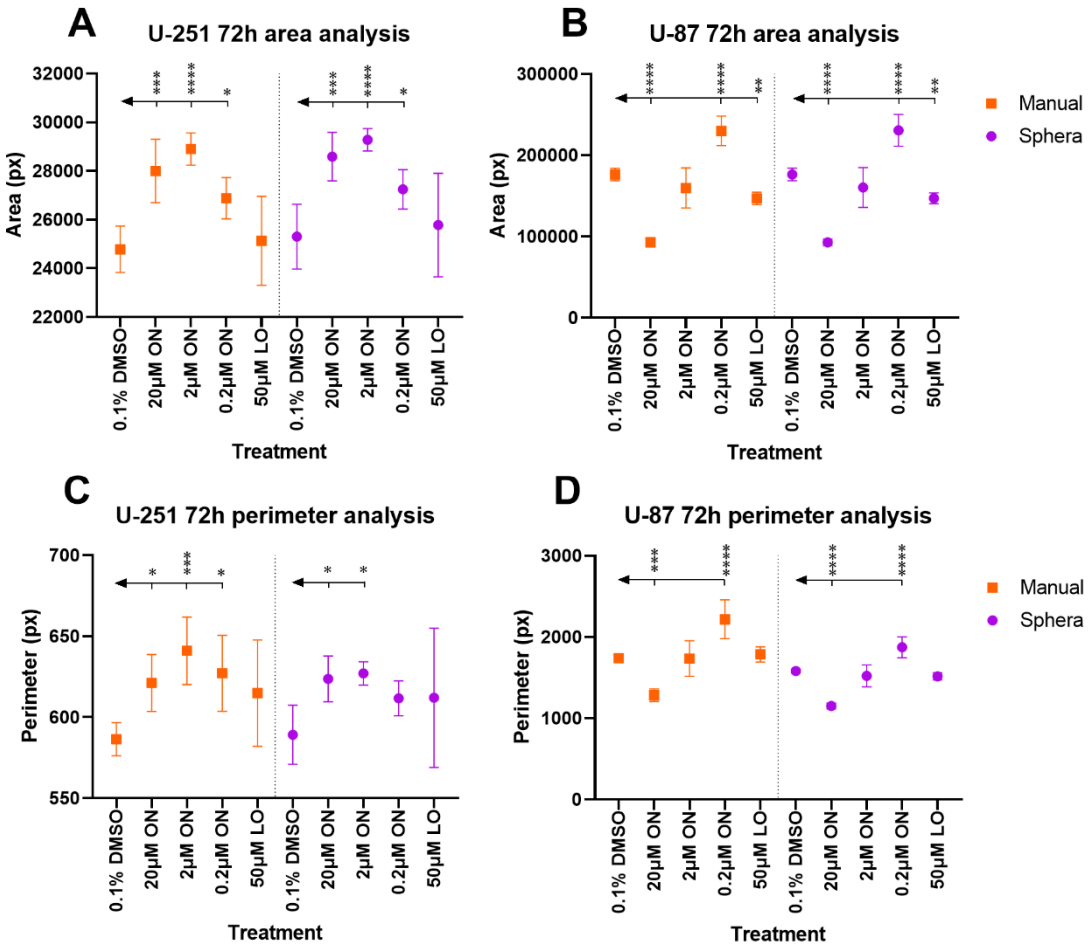

*Figure 7. Glioblastoma cell line U-251 and U-87 spheroid area (A, B) and perimeter (C. D) assessed at 72 hours after treatment with onametostat (ON) and lomustine (LO), both manually and with SpheraSense. The imaging scale was 1.613 µm/pixel. The data points plotted are an average of n = 6 measurements and the error bars are based on standard deviation. The negative control was treated with 0.1% DMSO and drug treatments included onametostat (20 µM, 2 µM, 0.2 µM) and lomustine (50 µM). Regarding significance assessed by one-way ANOVA, "***" indicates a p value of ≤ 0.001, "**" indicates p ≤ 0.01, and "*" stands for p ≤ 0.05.*

For the data analysis, the treated spheroids were compared to 0.1% DMSO controls, revealing that the cell lines U-251 and U-87 behaved quite differently with regard to spheroid size trends. For U-251, the spheroids at 72 hours (Figure 7.A) were significantly larger as a result of onametostat treatment, peaking at a concentration of 2 µM ($p < 0.001$). For U-87 cells (Figure 7.B), onametostat at a concentration of 0.2 µM significantly increased spheroid size, a concentration of 20 µM, however, had a strong effect ($p < 0.001$) of reducing spheroid area. In 72 hours, lomustine caused significantly ($p < 0.01$) smaller spheroids for the U-87 cells (Figure 7.B), but did not affect the U-

251 cell line (Figure 7.A), which was more chemotherapy resistant of the two cell lines. Area trends echoed in the perimeter data (Figure 7.C & D) and the significance trends were well captured with SpheraSense. As an exception, SpheraSense analysis resulted in a widely ranging error bars regarding the effect of 0.2 µM onametostat on U-251 spheroid perimeter (Figure 7.C), and resultingly, the software did not appoint significance to the drug effect contrary to manual assessment.

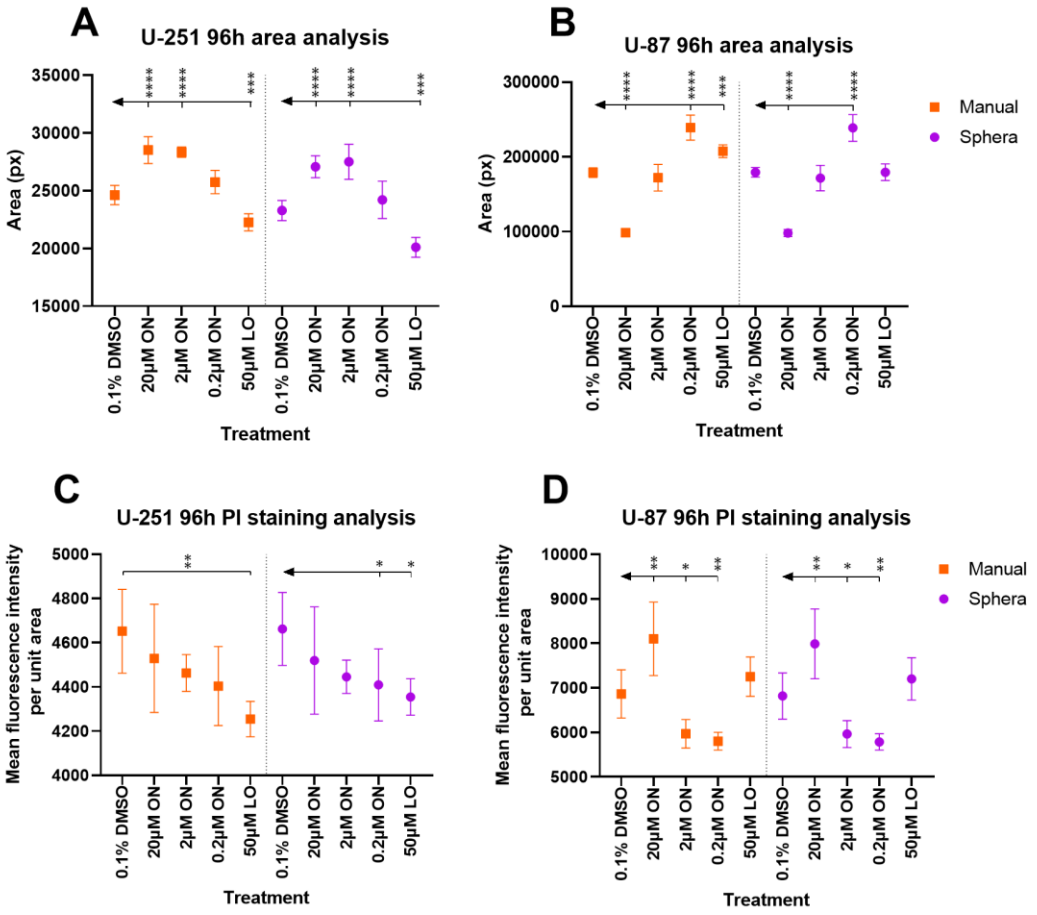

*Figure 8. Glioblastoma cell line U-251 and U-87 spheroid area (A, B) and propidium iodide staining (C, D) were assessed at 96 hours after treatment with onametostat (ON) and lomustine (LO), both manually and with SpheraSense. The imaging scale was 1.613 µm/pixel. The data points plotted are an average of n = 6 measurements and the error bars were based on standard deviation. The negative control was treated with 0.1% DMSO and drug treatments included onametostat (20 µM, 2 µM, 0.2 µM) and lomustine (50 µM). PI staining was quantified as a mean fluorescence intensity per unit area. Regarding significance assessed by one-way ANOVA, "***" indicates a p value of ≤ 0.001, "**" indicates p ≤ 0.01, and "*" stands for p ≤ 0.05.*

At the timepoint of 96 hours, the previously described area trends progressed and lomustine developed a significant effect on the U-251 cell line, reducing spheroid size (Figure 8.A). While lomustine reduced U-87 spheroid size at 72 hours (Figure 7.B), the effect seemed to reverse at 96 hours (Figure 8.B), producing significantly larger spheroids instead. Interestingly, SpheraSense did not appoint significance to the effect of lomustine on U-87 spheroid size in contrary to manual assessment (Figure 8.B).

PI staining revealed more cell death in the spheroid cells of the U-87 cell line (Figure 8.D), compared to U-251 (Figure 8.C), which was less affected by drug treatments. Overall, the drugs showed rather low in cytotoxicity while still having a considerable effect on spheroid formation, especially over a longer timeframe.

Regarding biological interpretation of the experiment, onametostat reliably increased spheroid sizes for U-251 without an effect on cell viability, suggesting that the drug disrupts cellular architecture rather than inducing cytotoxicity. Onametostat at a concentration of 20 μM, however, induced the most cancer cell death for the U-87 cell line, resulting in a significant area reduction.

Lomustine decreasing spheroid size of U-87 cells and at 96 hours also U-251 cells may result from hindered proliferation, adaptive resistance, or stress-induced spheroid decompaction, warranting further investigation. Although U-87 cells were expected to exhibit enhanced sensitivity to lomustine due to their negative MGMT expression status, the precise impact remains unclear, especially over a longer timeframe. Notably, the two cell lines responded rather differently, with onametostat at a low concentration of 0.2 μM often exerting a more pronounced effect than lomustine at 50 μM.

5.4 Validating the quality of SpheraSense based image analysis

To provide context for software performance, the deviation between the measurements of different researchers was assessed first with a small experiment. A dataset of 20 randomly picked bright-field microscopy images of spheroids was given to 3 researchers to be evaluated in terms of spheroid area, perimeter and circularity, using Fiji as described in the methods section of this work. To quantify the discrepancy of results, the coefficient of variation (CV) was calculated (Table 1).

Table 1. Coefficient of variance between researchers (n = 3) in evaluating spheroid area, perimeter and circularity. Data evaluated consisted of 20 bright-field microscopy images of randomly chosen spheroids.

	Average CV (%)	Max CV (%)	Min CV (%)
Area	3.3	15.9	0.7
Perimeter	18.5	38.6	2.8
Circularity	29.9	54.0	1.0

The results revealed that spheroid area measurements between researchers exhibited very low variability, with an average CV of 3.3%. In contrast, the perimeter and circularity measurements had higher overall variability, with average CV of 18.5% and 29.9%, respectively. As briefly mentioned, any discrepancy in the perimeter values is subject to significant amplification in circularity results (formula 1). The overall results, however, indicate that researcher interpretation in spheroid quantification may influence experimental outcomes in a considerable way.

Comparing the researchers' evaluations to SpheraSense (illustrated in Figure 9), the software adequately captured the patterns in the data of 20 spheroids, with the measurement results falling well within the range of variability observed among human interpretations (Table 1).

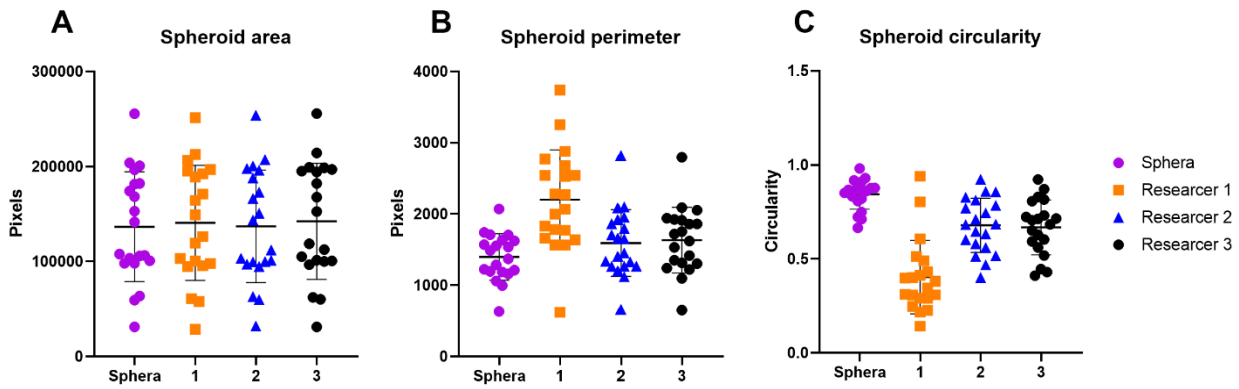

Figure 9. Comparison of the measurement results patterns produced by different researchers and SpheraSense. Visualized are the median value as the thick line in the middle of the clusters, the standard deviation of the measurements as plot whiskers, and every point on the graph represents a spheroid.

5.5 Evaluating software analysis on the cancer spheroid experiments

In the SCLC experiment, judging by the mean absolute percentage error (MAPE), the absolute differences between manual and software estimated datapoints averaged 12% in the case of spheroid area, 10% for perimeter data and 22% for circularity data. In assessing circularity in the SCLC experiment, SpheraSense seemed to underestimate irradiated spheroid circularity and overestimate the circularity of non-treated spheroids (Figure 4.C).

Regarding the HNSCC experiment, SpheraSense area analysis was highly similar to manual results – the average deviation from the manual area results by both area and perimeter was 2% judging by MAPE. In terms of circularity, the software differences from manual results averaged 5% with regards to 72-hour data and 6% regarding 96-hour data.

In the experiment employing GBM cell lines, SpheraSense replicated manual analysis well, with MAPE of 1% in spheroid area, 7% in perimeter and 18% in circularity quantification in terms of 72-hour glioblastoma data. MAPE with regard to 96-hour data was 4% in spheroid area, 10% in perimeter, 20% in circularity and 1% in PI staining quantification. Quantifying staining-based viability metrics was especially accurate. As an outlier result, the software did not capture the statistically important area increase of U-87 spheroids in response to lomustine at 96 hours, leaving room for improvement.

Summarizing the performance across three experiments, quantification of spheroid area and perimeter showed high accuracy, with mean absolute percentage errors typically below 10%. Circularity estimates were significantly more variable with up to 22% error in the SCLC experiment, yet remained directionally consistent with manual trends overall. Notably, the software achieved excellent accuracy across all measured parameters in the HNSCC experiment (max 6% error) and also in quantifying viability staining in the GBM experiment with 1% deviation. Collectively, the accuracy of SpheraSense in morphological assessments was highly comparable to human-level consistency, sufficient to detect significant outcomes, biological trends and draw experimental conclusions.

In terms of image dataset sizes, the FaDu experiment produced 60, SCLC 120 and GB 1140 images. The manual analysis times were 35 minutes for FaDu, 1 hour for SCLC and as the GBM data was unreasonably extensive to quantify by hand, a subset of 120 images was quantified in an hour, approximately. Running SpheraSense took 6 minutes for both HNSCC and SCLC, and ~50 minutes for the full GBM experiment analysis. The average quantification speed, therefore, was 1.9 images/min manually and 17.2 images/min for the software, which was a ninefold increase in processing efficiency. It must be noted that this performance was achieved using a regular laptop and not a dedicated computational cluster.

Regarding the ease of integration into established workflows, SpheraSense was simply installed as a MATLAB application and read microscopy images and associated metadata straight from the shared NOMERO image filesystem, needing no additional setup.

6. SUMMARY

Improving the scalability and reproducibility of experimental work is critical for advancing translational research. Spheroid cell cultures have become indispensable in cancer research for their ability to more accurately model tumor behavior and drug response than traditional 2D cell culturing systems.

In this thesis, the tool SpheraSense was developed, which was based on MATLAB and integrated Ilastik for training and running machine learning models for spheroid segmentation. As proof-of-concept, SpheraSense was applied to quantify microscopy images from three spheroid experiments using cancerous cell lines – small-cell lung cancer CRL-5853, head and neck cancer FaDu and glioblastoma lines U-251 and U-87. Each experiment subjected spheroids to distinct cancer treatments including irradiation, immunotherapeutic drugs (nivolumab, pembrolizumab), chemotherapeutic drug (lomustine) and an investigational drug candidate onametostat.

SpheraSense quantified both morphological and fluorescence features of cancer spheroids, matched human-level consistency that was tested with a small experiment and captured most of the important qualitative and quantitative experiment trends and effects. Quantifying the spheroid perimeter was subject to significantly larger variability than the area predictions. Regarding robustness, the software reliably detected significant findings in morphological data while reducing analysis time by a factor of nine, on average, under field conditions. Taken together, SpheraSense offers an efficient alternative to manual quantification of spheroid cell culture experiments with flexible and user-friendly integration into pre-existing workflows.

KOKKUVÕTE

Katseandmete töötluse skaleeritavuse ja reprodutseeritavuse parandamine on kriitilise tähtsusega rakendusliku teaduse arendamisel. Sferoidsete rakukultuuride kasutamine on vähi uurimisel muutunud asendamatuks, simuleerides kasvajate käitumist ja ravivastust täpsemalt kui traditsioonilised kahemõõtmelised rakukultuurisüsteemid.

Käesolevas töös arendati tööriist SpheraSense, mis põhineb MATLAB-il ning integreerib Ilastiku masinõppemudelite treenimiseks ja sferoidide segmenteerimiseks. Tõestamaks kontseptsiooni rakendatavust, kasutati SpheraSense'i kolme erineva sferoidkatse mikroskoopiapiltide kvantifitseerimiseks, kasutades väikerakse kopsuvähi liini CRL-5853, pea- ja kaelapiirkonna vähi liini FaDu, ning glioblastoomide liine U-251 ja U-87. Katsetes puutusid sferoidid kokku erinevate vähiravimeetoditega, sealhulgas kiiritus, immuunravi (nivolumab, pembrolizumab), keemiaravi (lomustiin) ning sihtmärkravi kadidaatühend (onametostat).

SpheraSense kvantifitseeris nii morfoloogilisi kui ka fluorestsentsipõhiseid tunnuseid, saavutas inimtasemele lähedase järjepidevuse (kontrollitud katselise võrdluse abil) ning tuvastas valdava enamuse statistiliselt olulistest kvalitatiivsetest ja kvantitatiivsetest katsetulemustest. Sferoidi perimeetri kvantifitseerimise täpsus osutus seejuures oluliselt varieeruvamaks kui pindala hindamine. Tarkvara oli morfoloogiliste leidude tuvastamisel töökindel ning vähendas keskmiselt andmeanalüüsile kuluvat aega üheksakordselt. Kokkuvõttes pakub SpheraSense tõhusat ja paindlikku alternatiivi sferoidide manuaalsele kvantifitseerimisele ning sobitub hästi olemasolevatesse töövoogudesse.

ACKNOWLEGEMENTS

I thank all the people who have contributed to the completion of my bachelor's studies and thesis. Special appreciation goes to my thesis supervisors Darja Lavõgina and Tõnis Laasfeld, brilliant in both their scientific rigor and mentorship, providing engaging discussions and expert guidance that shaped this project. I am grateful for having had the opportunity to collaborate with you and continue to be deeply inspired by the research you both lead.

I also extend my sincere thanks to the University of Tartu for providing me with a strong educational foundation and practical competence, preparing me for a fulfilling career of tackling scientific challenges.

REFERENCES

[1] W. Roux, ‘Beiträge zur Entwickelungsmechanik des Embryo’, *Arch. Für Pathol. Anat. Physiol. Für Klin. Med.*, vol. 114, no. 1, pp. 113–153, Oct. 1888, doi: 10.1007/BF01935891.

[2] J.-P. Gillet, S. Varma, and M. M. Gottesman, ‘The Clinical Relevance of Cancer Cell Lines’, *JNCI J. Natl. Cancer Inst.*, vol. 105, no. 7, pp. 452–458, Apr. 2013, doi: 10.1093/jnci/djt007.

[3] ‘Cancer Cell Line Encyclopedia (CCLE)’, Cancer Cell Line Encyclopedia (CCLE). Accessed: Dec. 20, 2024. [Online]. Available: https://sites.broadinstitute.org/ccle/

[4] L. G. Moro *et al.*, ‘A Brief History of Cell Culture: From Harrison to Organs-on-a-Chip’, *Cells*, vol. 13, no. 24, Art. no. 24, Jan. 2024, doi: 10.3390/cells13242068.

[5] M. A. G. Barbosa, C. P. R. Xavier, R. F. Pereira, V. Petrikaitė, and M. H. Vasconcelos, ‘3D Cell Culture Models as Recapitulators of the Tumor Microenvironment for the Screening of Anti-Cancer Drugs’, *Cancers*, vol. 14, no. 1, Art. no. 1, Jan. 2022, doi: 10.3390/cancers14010190.

[6] ‘(PDF) Trypsin-induced proteome alteration during cell subculture in mammalian cells’, *ResearchGate*, Oct. 2024, doi: 10.1186/1423-0127-17-36.

[7] Y. Kurashina *et al.*, ‘Enzyme-free release of adhered cells from standard culture dishes using intermittent ultrasonic traveling waves’, *Commun. Biol.*, vol. 2, no. 1, pp. 1–11, Oct. 2019, doi: 10.1038/s42003-019-0638-5.

[8] D. Lv, Z. Hu, L. Lu, H. Lu, and X. Xu, ‘Three-dimensional cell culture: A powerful tool in tumor research and drug discovery’, *Oncol. Lett.*, vol. 14, no. 6, pp. 6999–7010, Dec. 2017, doi: 10.3892/ol.2017.7134.

[9] N. U. B. Hansen, F. Genovese, D. J. Leeming, and M. A. Karsdal, ‘The importance of extracellular matrix for cell function and in vivo likeness’, *Exp. Mol. Pathol.*, vol. 98, no. 2, pp. 286–294, Apr. 2015, doi: 10.1016/j.yexmp.2015.01.006.

[10] Y. Park, K. M. Huh, and S.-W. Kang, ‘Applications of Biomaterials in 3D Cell Culture and Contributions of 3D Cell Culture to Drug Development and Basic Biomedical Research’, *Int. J. Mol. Sci.*, vol. 22, no. 5, Art. no. 5, Jan. 2021, doi: 10.3390/ijms22052491.

[11] K. Białkowska, P. Komorowski, M. Bryszewska, and K. Miłowska, ‘Spheroids as a Type of Three-Dimensional Cell Cultures—Examples of Methods of Preparation and the Most Important Application’, *Int. J. Mol. Sci.*, vol. 21, no. 17, p. 6225, Aug. 2020, doi: 10.3390/ijms21176225.

[12] S. G. Anthon and K. P. Valente, ‘Vascularization Strategies in 3D Cell Culture Models: From Scaffold-Free Models to 3D Bioprinting’, *Int. J. Mol. Sci.*, vol. 23, no. 23, Art. no. 23, Jan. 2022, doi: 10.3390/ijms232314582.

[13] M. E. Katt, A. L. Placone, A. D. Wong, Z. S. Xu, and P. C. Searson, ‘In Vitro Tumor Models: Advantages, Disadvantages, Variables, and Selecting the Right Platform’, *Front. Bioeng. Biotechnol.*, vol. 4, Feb. 2016, doi: 10.3389/fbioe.2016.00012.

[14] A. C. Debruyne *et al.*, ‘Live Microscopy of Multicellular Spheroids with the Multimodal Near-Infrared Nanoparticles Reveals Differences in Oxygenation Gradients’, *ACS Nano*, vol. 18, no. 19, pp. 12168–12186, Apr. 2024, doi: 10.1021/acsnano.3c12539.

[15] ‘Environmental control of mammary carcinoma cell expansion by acidification and spheroid formation in vitro | Scientific Reports’. Accessed: May 18, 2025. [Online]. Available: https://www.nature.com/articles/s41598-020-78989-6
[16] A. Tafech, P. Jacquet, C. Beaujean, A. Fertin, Y. Usson, and A. Stéphanou, ‘Characterization of the Intracellular Acidity Regulation of Brain Tumor Cells and Consequences for Therapeutic Optimization of Temozolomide’, *Biology*, vol. 12, no. 9, p. 1221, Sep. 2023, doi: 10.3390/biology12091221.
[17] A. del M. B. Garnique, N. S. Parducci, L. B. L. de Miranda, B. O. de Almeida, L. Sanches, and J. A. Machado-Neto, ‘Two-Dimensional and Spheroid-Based Three-Dimensional Cell Culture Systems: Implications for Drug Discovery in Cancer’, *Drugs Drug Candidates*, vol. 3, no. 2, Art. no. 2, Jun. 2024, doi: 10.3390/ddc3020024.
[18] P. Vaupel, ‘Tumor microenvironmental physiology and its implications for radiation oncology’, *Semin. Radiat. Oncol.*, vol. 14, no. 3, pp. 198–206, Jul. 2004, doi: 10.1016/j.semradonc.2004.04.008.
[19] S. M. Roy, V. Garg, S. Barman, C. Ghosh, A. R. Maity, and S. K. Ghosh, ‘Kinetics of Nanomedicine in Tumor Spheroid as an In Vitro Model System for Efficient Tumor-Targeted Drug Delivery With Insights From Mathematical Models’, *Front. Bioeng. Biotechnol.*, vol. 9, Dec. 2021, doi: 10.3389/fbioe.2021.785937.
[20] E. Gheytanchi *et al.*, ‘Morphological and molecular characteristics of spheroid formation in HT-29 and Caco-2 colorectal cancer cell lines’, *Cancer Cell Int.*, vol. 21, no. 1, p. 204, Apr. 2021, doi: 10.1186/s12935-021-01898-9.
[21] A. F. Farago and F. K. Keane, ‘Current standards for clinical management of small cell lung cancer’, *Transl. Lung Cancer Res.*, vol. 7, no. 1, Feb. 2018, doi: 10.21037/tlcr.2018.01.16.
[22] ‘(PDF) Comparison of Radiation Response between 2D and 3D Cell Culture Models of Different Human Cancer Cell Lines’, *ResearchGate*, May 2025, doi: 10.3390/cells12030360.
[23] Y. Zhang and Z. Zhang, ‘The history and advances in cancer immunotherapy: understanding the characteristics of tumor-infiltrating immune cells and their therapeutic implications’, *Cell. Mol. Immunol.*, vol. 17, no. 8, pp. 807–821, Aug. 2020, doi: 10.1038/s41423-020-0488-6.
[24] K. X. Lin, A. C. Istl, D. Quan, A. Skaro, E. Tang, and X. Zheng, ‘PD-1 and PD-L1 inhibitors in cold colorectal cancer: challenges and strategies’, *Cancer Immunol. Immunother. CII*, vol. 72, no. 12, pp. 3875–3893, Oct. 2023, doi: 10.1007/s00262-023-03520-5.
[25] P. Fessas, H. Lee, S. Ikemizu, and T. Janowitz, ‘A molecular and preclinical comparison of the PD-1–targeted T-cell checkpoint inhibitors nivolumab and pembrolizumab’, *Semin. Oncol.*, vol. 44, no. 2, pp. 136–140, Apr. 2017, doi: 10.1053/j.seminoncol.2017.06.002.
[26] Y. Han, D. Liu, and L. Li, ‘PD-1/PD-L1 pathway: current researches in cancer’, *Am. J. Cancer Res.*, vol. 10, no. 3, pp. 727–742, Mar. 2020.
[27] M. Saar, D. Lavogina, H. Lust, H. Tamm, and J. Jaal, ‘Immune checkpoint inhibitors modulate the cytotoxic effect of chemotherapy in lung adenocarcinoma cells’, *Oncol. Lett.*, vol. 25, no. 4, p. 152, Mar. 2023, doi: 10.3892/ol.2023.13738.
[28] M. Saar *et al.*, ‘Exploring the Molecular Players behind the Potentiation of Chemotherapy Effects by Durvalumab in Lung Adenocarcinoma Cell Lines’, *Pharmaceutics*, vol. 15, no. 5, p. 1485, May 2023, doi: 10.3390/pharmaceutics15051485.

[29] G. V. Long *et al.*, ‘Assessment of nivolumab exposure and clinical safety of 480 mg every 4 weeks flat-dosing schedule in patients with cancer’, *Ann. Oncol.*, vol. 29, no. 11, pp. 2208–2213, Nov. 2018, doi: 10.1093/annonc/mdy408.
[30] P. Sachamitr *et al.*, ‘PRMT5 inhibition disrupts splicing and stemness in glioblastoma’, *Nat. Commun.*, vol. 12, p. 979, Feb. 2021, doi: 10.1038/s41467-021-21204-5.
[31] D. Lavogina *et al.*, ‘Inhibition of epigenetic and cell cycle-related targets in glioblastoma cell lines reveals that onametostat reduces proliferation and viability in both normoxic and hypoxic conditions’, *Sci. Rep.*, vol. 14, no. 1, p. 4303, Feb. 2024, doi: 10.1038/s41598-024-54707-4.
[32] M. Weller and E. Le Rhun, ‘How did lomustine become standard of care in recurrent glioblastoma?’, *Cancer Treat. Rev.*, vol. 87, p. 102029, Jul. 2020, doi: 10.1016/j.ctrv.2020.102029.
[33] M. E. Hegi *et al.*, ‘MGMT Gene Silencing and Benefit from Temozolomide in Glioblastoma’, *N. Engl. J. Med.*, vol. 352, no. 10, pp. 997–1003, Mar. 2005, doi: 10.1056/NEJMoa043331.
[34] ‘Dunkle: Role of image informatics in accelerating... - Google Scholar’. Accessed: Mar. 29, 2025. [Online]. Available: https://scholar.google.com/scholar_lookup?journal=Drug%20Discovery&title=Role%20of%20image%20informatics%20in%20accelerating%20drug%20discovery%20and%20development&author=R%20Dunkle&volume=4&publication_year=2003&pages=75-82&
[35] M. Jan, A. Spangaro, M. Lenartowicz, and M. Mattiazzi Usaj, ‘From pixels to insights: Machine learning and deep learning for bioimage analysis’, *BioEssays*, vol. 46, no. 2, p. 2300114, 2024, doi: 10.1002/bies.202300114.
[36] S. Kothari, J. H. Phan, T. H. Stokes, and M. D. Wang, ‘Pathology imaging informatics for quantitative analysis of whole-slide images’, *J. Am. Med. Inform. Assoc. JAMIA*, vol. 20, no. 6, pp. 1099–1108, Nov. 2013, doi: 10.1136/amiajnl-2012-001540.
[37] A. Zwanenburg, S. Leger, M. Vallières, and S. Löck, ‘Image biomarker standardisation initiative’, *Radiology*, vol. 295, no. 2, pp. 328–338, May 2020, doi: 10.1148/radiol.2020191145.
[38] Z. He and W. Yu, ‘Stable feature selection for biomarker discovery’, *Comput. Biol. Chem.*, vol. 34, no. 4, pp. 215–225, Aug. 2010, doi: 10.1016/j.compbiolchem.2010.07.002.
[39] I. H. Sarker, ‘Machine Learning: Algorithms, Real-World Applications and Research Directions’, *SN Comput. Sci.*, vol. 2, no. 3, p. 160, Mar. 2021, doi: 10.1007/s42979-021-00592-x.
[40] E. Moen, D. Bannon, T. Kudo, W. Graf, M. Covert, and D. Van Valen, ‘Deep learning for cellular image analysis’, *Nat. Methods*, vol. 16, no. 12, pp. 1233–1246, Dec. 2019, doi: 10.1038/s41592-019-0403-1.
[41] T. Haigh, ‘Cleve Moler: Mathematical Software Pioneer and Creator of Matlab’, *IEEE Ann. Hist. Comput.*, vol. 30, no. 1, pp. 87–91, Jan. 2008, doi: 10.1109/MAHC.2008.2.
[42] S. Berg *et al.*, ‘ilastik: interactive machine learning for (bio)image analysis’, *Nat. Methods*, vol. 16, no. 12, pp. 1226–1232, Dec. 2019, doi: 10.1038/s41592-019-0582-9.
[43] J. Schindelin *et al.*, ‘Fiji: an open-source platform for biological-image analysis’, *Nat. Methods*, vol. 9, no. 7, pp. 676–682, Jul. 2012, doi: 10.1038/nmeth.2019.
[44] C. A. Schneider, W. S. Rasband, and K. W. Eliceiri, ‘NIH Image to ImageJ: 25 years of image analysis’, *Nat. Methods*, vol. 9, no. 7, pp. 671–675, Jul. 2012, doi: 10.1038/nmeth.2089.

[45] ‘Scientific Image and Illustration Software | BioRender’. Accessed: Mar. 29, 2025. [Online]. Available: https://www.biorender.com/

ANNEXES

1. Plating scheme and imaging results of the SCLC experiment

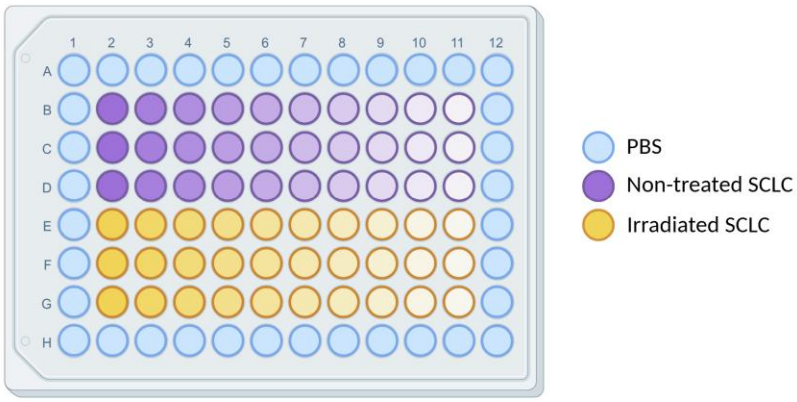

Figure 10. 96-well plate layout used for small-cell lung cancer spheroid experiment.

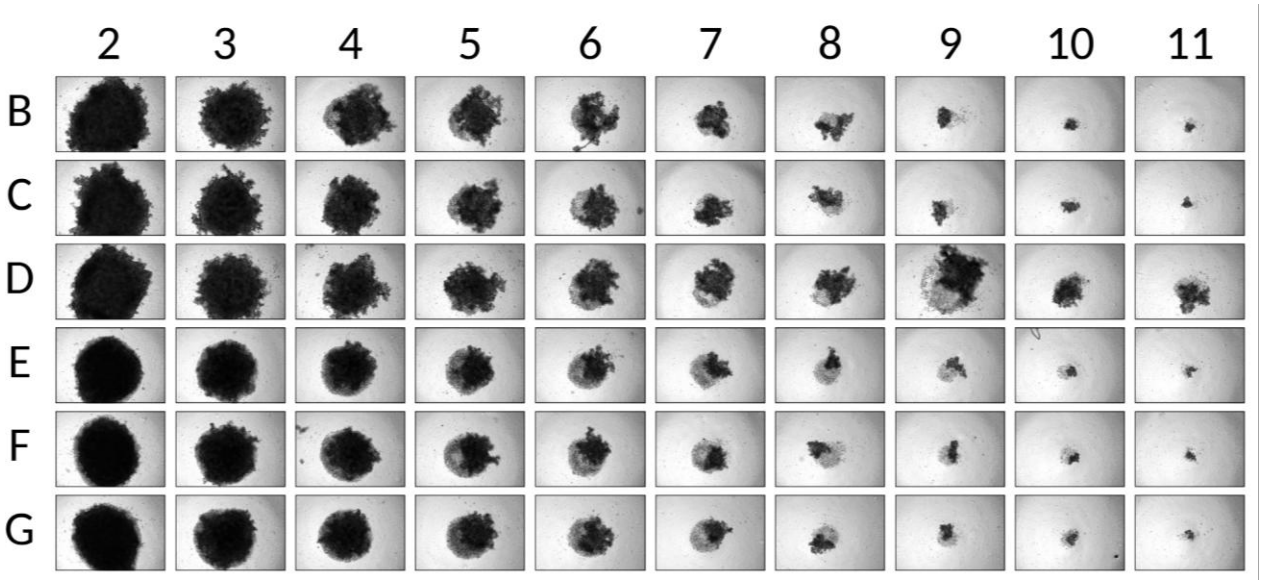

Figure 11. Small-cell lung cancer spheroids 72 hours post-seeding. The real scale of the microscopy images is approximately 1500 x 2000 microns.

2. Plating scheme and imaging results of the HNSCC experiment

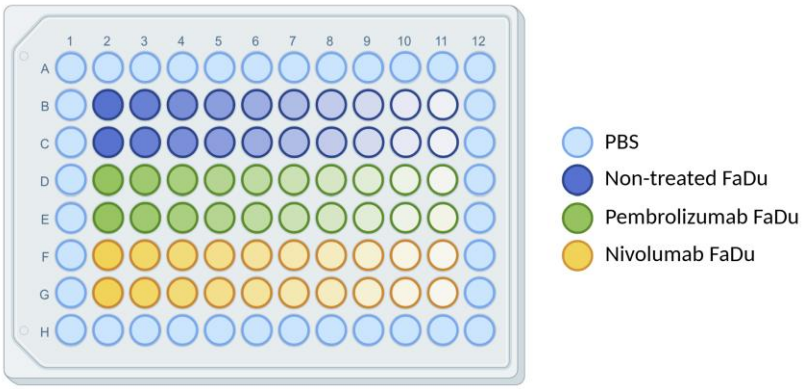

Figure 12. 96-well plate layout used for the FaDu spheroid experiment.

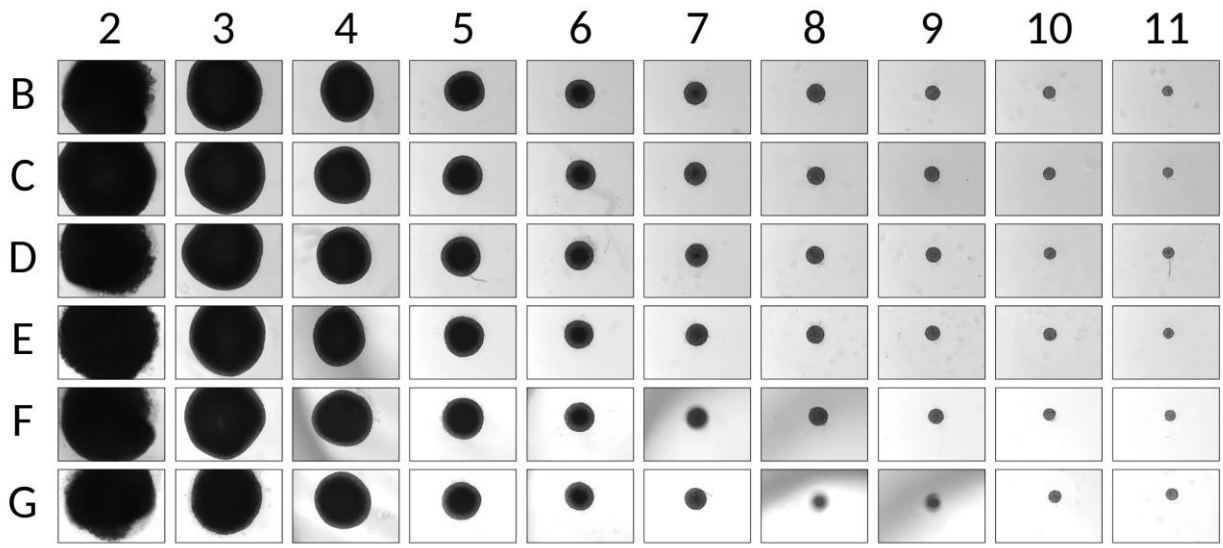

Figure 13. FaDu experiment imaged 72 hours post-seeding. The real scale of the microscopy images is approximately 1500 x 2000 microns.

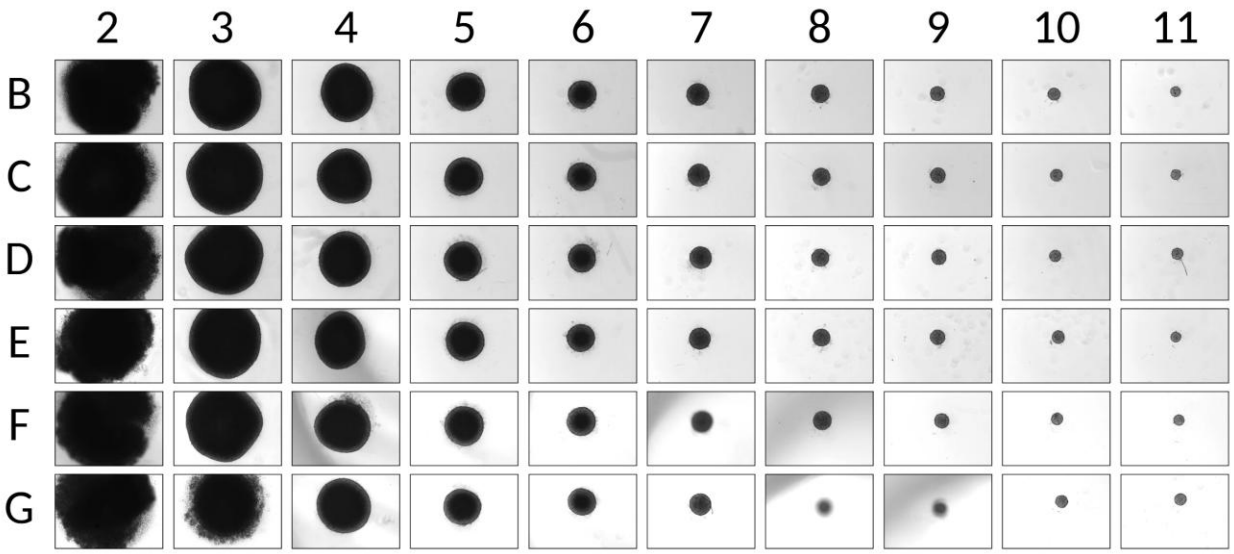

Figure 14. FaDu experiment imaged 96 hours post-seeding. The real scale of the microscopy images is approximately 1500 x 2000 microns.

3. Plating scheme and imaging results of the GBM experiment

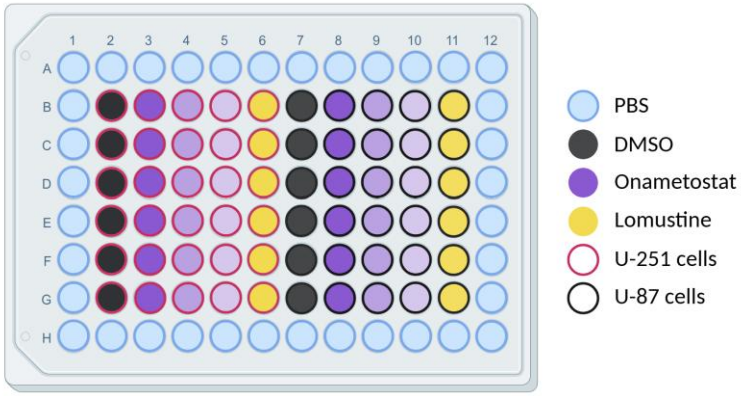

Figure 15. 96-well plate layout used for the glioblastoma spheroid experiment.

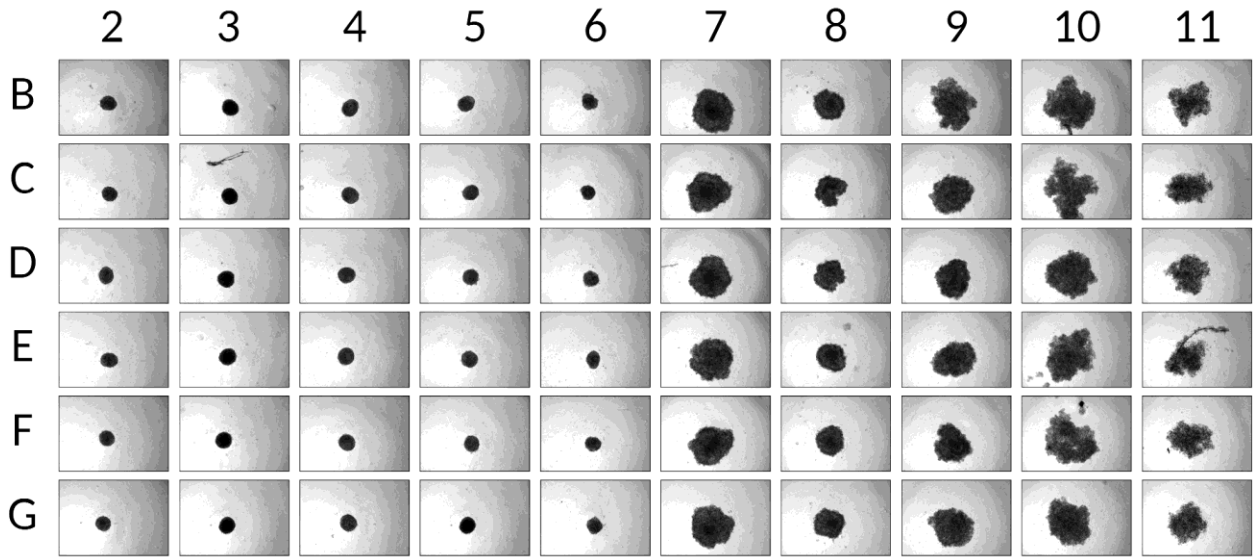

Figure 16. Glioblastoma (U-251 and U-87) spheroids 72 hours post seeding. The real scale of the microscopy images is approximately 1500 x 2000 microns.

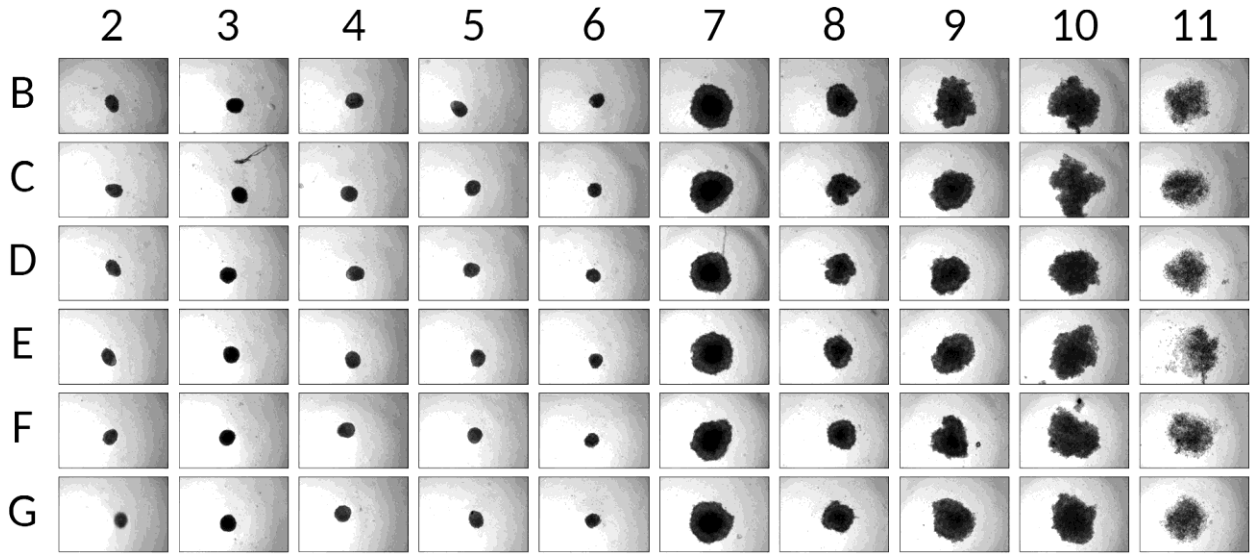

Figure 17. Glioblastoma (U-251 and U-87) spheroids 96 hours post seeding. The real scale of the microscopy images is approximately 1500 x 2000 microns.

4. SpheraSense installation and walk-through

Requirements

- MATLAB along with
    - 'Image Processing Toolbox'
    - 'Statistics and Machine Learning Toolbox'
- Ilastik for running the machine learning model

Interface guide

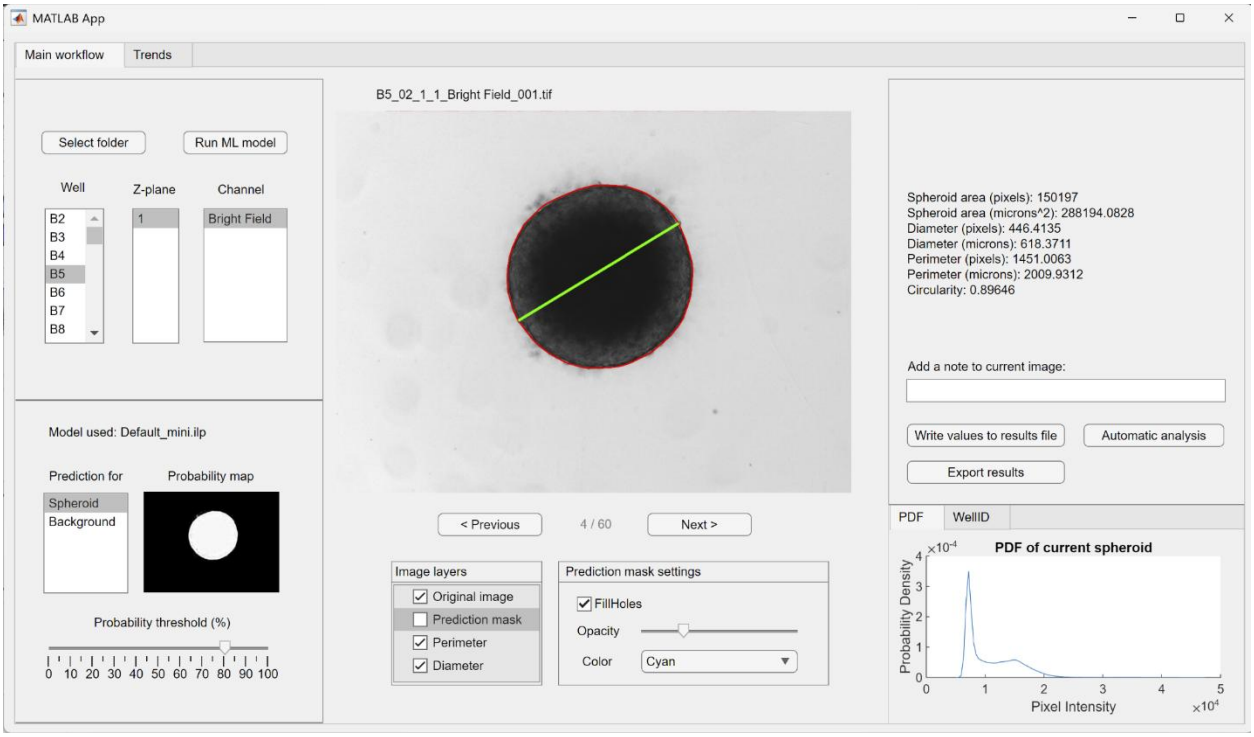

Figure 18. SpheraSense interface.

Left hand panels:

'Select folder' Prompts the choice of folder of images to be analysed.

‘Run ML model’ Prompts the choice of an HDF5 machine learning model file to be used in analysis.

‘Well’, **‘Z-plane’** and **‘Channel’** are used for browsing and navigation of images across their well IDs of a 96-well plate (A1-H12), imaging Z-stack planes and imaging channels.

‘Prediction for’ References ML prediction labels the model was trained to recognize.

‘Probability map’ Shows ML prediction output - visualised confidence of spheroid detection.

‘Probability threshold’ Slider changes the prediction confidence level to adjust the detected area.

Center area:

‘Image’ In the middle of the interface is the original image currently analysed.

‘Previous’ and **‘Next’** Serve for browsing the images in the folder under analysis.

‘Image layers’ Are used to visualize the quantification of different parameters.

‘**Prediction mask settings’** Are useful to visualize the spheroid in different imaging channels.

Right hand panels:

‘Spheroid quantification data’ Displays quantification results or warnings/requests for the user.

‘PDF graph’ is a probability density function, plots pixel intensities against their relative abundance (%) concerning only the spheroid area.

‘Note taking box’ Enables attaching a note to the current image. Useful for flagging contamination.

‘Write values to results file’ Writes the image info currently displayed in the export file as a row.

‘**Export results**’ Finalizes the data into an .csv/xsl file.

‘**Automatic analysis**’ With the threshold specified, automatically analyses all the images in the folder and exports with the user preferred format and filename.

Workflow and troubleshooting:

1. **Download SpheraSense**

SpheraSense is publicly available on GitHub. Ensure its requirements are met and open it in MATLAB.

2. **Select folder**

Prompts the choice of folder of microscopy images which are to be analysed. A smaller folder may be preferable for testing different ML models. The warning "No microscopy images in the selected folder" implies no microscopy images are found (e.g., the initially chosen folder might contain subfolders - please go to the subfolder level). The software may also report files with "unexpected filenames" in which case the filename is not structured as follows: *WellID_ReadIndex_ChannelIndex_ZIndex_ChannelName_CycleIndex*. If the image files do not conform to this naming convention, please use a microscopy image filename converter to reformat them accordingly.

3. **Run a machine learning model**

Prompts the choice of a pre-trained machine learning model (HDF5 file) that will be used in analysis. The software does not yet handle other ML model files. The software uses **Ilastik** to run the prediction part of the workflow, resulting in h5 probability files.

When finished, SpheraSense looks for labels 'Spheroid' and 'Background' in the trained model but can visualize any other labels used.

4. **Browse**

Get a sense of the data, browse wells and Z-planes. Visualized measurements of the spheroid are displayed - perimeter in red, diameter in green, prediction mask in a user preferred manner.

In the case of an RFP/DAPI/CY5 image, the software assumes there is a corresponding bright-field image available, from which the spheroid is detected.

5. **Analyse and export results**

- Manual analysis

  For datasets from which only specific wells need to be analysed, the user may navigate between different images and click ‘Write values to file’ (which also navigates to the next image) and when finished, on ‘Export’. The data about what is currently written in the results file is available in the MATLAB terminal.

- Automatic analysis

  For large datasets that can be analysed with a set threshold, ‘Automatic analysis’ goes through all images, quantifies them and exports the results file automatically, simply asking for the results file name. The progress can be observed in the MATLAB terminal.

5. Licence

Non-exclusive licence to reproduce the thesis and make the thesis public

I, Margaret Pütsepp,

1. grant the University of Tartu a free permit (non-exclusive licence) to reproduce, for the purpose of preservation, including adding to the digital archives of the University of Tartu until the expiry of the term of copyright, my thesis

"SpheraSense: A Software Tool to Automate and Standardize the Analysis of Cancer Spheroid Microscopy Images"

supervised by PhD Tõnis Laasfeld and PhD Darja Lavõgina

2. make the thesis specified in point 1 available to the public via the web environment of the University of Tartu, including via the digital archives, under the Creative Commons licence CC BY NC ND 4.0, which allows, by giving appropriate credit to the author, to reproduce, distribute the work and communicate it to the public, and prohibits the creation of derivative works and any commercial use of the work from 20.05.2025 until the expiry of the term of copyright;
3. am aware that the author retains the rights specified in points 1 and 2;
4. confirm that granting the non-exclusive licence does not infringe other persons' intellectual property rights or rights arising from the personal data protection legislation.

Tartu

20.05.2025